The Effects of Cathodic Reagent Concentration and Small Solution Volumes on the Corrosion of Copper in Dilute Nitric Acid Solutions

J. Turnbull,[‡,*] R. Szukalo,[*] M. Behazin,[*] D. Hall,[**] D. Zagidulin,[*] S. Ramamurthy,[***] J.C. Wren,[*] and D.W. Shoesmith[*,***]

ABSTRACT

The exposure conditions experienced by copper-coated high-level nuclear waste containers in a deep geologic repository will evolve with time. An early exposure period involving the gamma irradiation of aerated humid vapor could lead to the formation of nitric acid condensed in limited volumes of water on the container surface. The evolution of the corrosion processes under these conditions have been studied using pH measurements in limited volumes of water containing various concentrations of nitric acid. The extent and morphology of corrosion was examined using scanning electron microscopy on surfaces and on focused ion beam cut cross sections. The composition of corrosion products was determined by energy dispersive x-ray analyses and Raman spectroscopy. In the absence of dissolved oxygen only minor corrosion was observed with the reduction of nitric acid inhibited by the formation of either chemisorbed nitrate and nitrite species or the formation of a thin cuprite (Cu_2O) layer. When the solution was aerated, both oxygen and nitric acid acted as cathodic reagents. After extensive exposure periods corrosion was stifled by the formation of corrosion product deposits of Cu_2O, CuO (tenorite), and $Cu_2NO_3(OH)_3$ (rouaite).

KEY WORDS: copper, copper oxides, corrosion rate, nitric acid, nitrous acid, nuclear waste containers, pH, rouaite, small solution volumes

INTRODUCTION

The internationally accepted method for the permanent disposal of high-level nuclear waste, which is currently under consideration in Canada, is burial in a deep geologic repository (DGR) at a depth of ≥500 m in a suitably dense intact rock, Figure 1. To ensure containment, the fuel waste form will be sealed in a corrosion resistant container designed to withstand the anticipated hydrostatic, lithostatic, and glacial loads. The original container design was similar to the Scandinavian KBS-3 container, comprising an inner steel vessel protected against corrosion by a 25 mm to 50 mm thick Cu outer shell.[1] However, corrosion models predict that the maximum corrosion penetration in a Canadian DGR will be <1.27 mm over 10^6 y.[2-3]

With this in mind, and to overcome design and fabrication issues, a thinner-walled Cu-coated container is being investigated.[4] This has stimulated a re-evaluation of the container corrosion performance, in particular whether or not radiolytic oxidants, produced by the gamma (ϒ) radiation emitted by the decay of radionuclides in the spent fuel wasteform, will lead to meaningful amounts of corrosion damage. For a thick-walled container, ϒ-radiation fields at the outer surface of the container (≪1 Gy/h) were considered unimportant because their influence on corrosion would be negligible.[5] However, for the thin-walled

Submitted for publication: September 13, 2017. Revised and accepted: October 30, 2017. Preprint available online: October 30, 2017, https://doi.org/10.5006/2655.
‡ Corresponding author. E-mail: jturnbu2@uwo.ca.
* University of Western Ontario, Department of Chemistry, 1151 Richmond St., London, Ontario, Canada, N6A 5B7.
** Nuclear Waste Management Organization, 22 St. Claire Avenue East, 6th Floor, Toronto, Ontario, Canada, M4T 2S3.
*** University of Western Ontario, Surface Science Western, 999 Collip Circle, London, Ontario, Canada, N6G 0J3.

ISSN 0010-9312 (print), 1938-159X (online)
18/000053/$5.00+$0.50/0

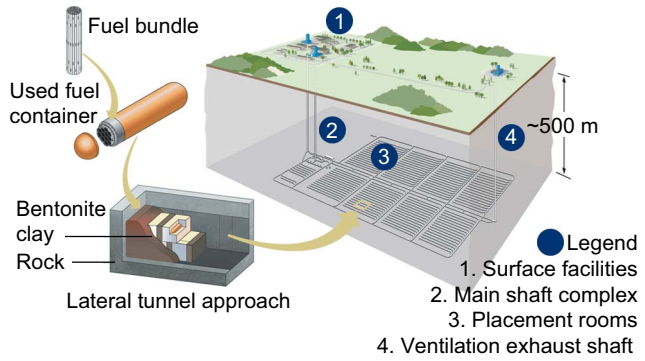

FIGURE 1. *Schematic illustration of the proposed Canadian DGR showing how the used fuel bundles would be sealed in a Cu-coated steel vessel and emplaced in engineered tunnels with the region around the container filled with bentonite clay blocks and the residual space backfilled with a clay/crushed rock mixture. The general layout of the DGR is illustrated by the features 1 to 4.*

coated container, the ϒ-dose rate at this location will be increased by a factor of >20, and is calculated to decay from ~2.3 Gy/h to ~0.02 Gy/h over 200 y.[6] As a consequence, a more thorough analysis of the possible influence of radiation on corrosion damage is required.

Upon sealing the DGR, the temperature of the container surface will rise as a result of the heat produced by the radioactive decay processes. Initially, this will produce a low humidity environment in the vicinity of the container and negligible corrosion would be anticipated. Subsequently, moisture will return as the containers cool, allowing the local relative humidity (RH) to exceed the critical value required to establish aqueous conditions, leading to the onset of atmospheric corrosion.[7] The period required to establish full saturation of the near field (i.e., the compacted clay close to the container surface) will depend on the site-specific hydraulic conductivity of the host rock, and is currently estimated to be ~50 y (for crystalline rock) or ~5,000 y (for a sedimentary host rock).[8]

As saturation occurs, the prospects for corrosion increase, and four different, but not necessarily separated, container exposure periods can be defined:[9] (i) aerated vapor but no condensed H_2O on the Cu surface; (ii) aerated vapor in equilibrium with condensed H_2O; (iii) anoxic, or close-to-anoxic, conditions with either H_2O vapor in equilibrium with condensed H_2O or a fully saturated condition; and (iv) a fully anoxic, H_2O-saturated condition. During this evolution, the redox conditions at the Cu surface will be significantly influenced by the ϒ-radiation field which will produce oxidants in both aqueous vapor and condensed H_2O. This study is primarily concerned with the period when a combination of aerated vapor and condensed water exists at the container surface. Under these conditions the radiolysis of the aerated vapor will produce HNO_3,[10-12] which will be absorbed into condensed H_2O in contact with the aerated vapor.[13-15]

The effect of radiation on the corrosion of Cu has been studied in both aqueous solutions[16-23] and in humid air,[24] usually at dose rates well in excess of those anticipated on a container surface, but with contrasting observations. In both aerated and deaerated chloride solutions (150°C, 27 Gy/h), radiation appeared to be beneficial, leading to the formation of an apparently protective Cu_2O film.[18-19] In the absence of radiation, the film was fractured and contained $CuCl_3{\cdot}3Cu(OH)_2$ indicating breakdown of the Cu_2O layer and the deposition of Cu^{2+} solids. At higher dose rates (80 Gy/h to 770 Gy/h), more extensive corrosion was observed with the deposited corrosion product film (predominantly Cu_2O) thought to play a significant role in amplifying the influence of ϒ-radiation.[23]

Under unsaturated aerated conditions more relevant to these studies, modest dose rates (100 Gy/h [90°C to 150°C])[24] also lead to the formation of an apparently protective Cu_2O layer, the corrosion rate being only marginally greater (~1.5 times) than that in the absence of radiation. At a higher dose rate (700 Gy/h), cupric nitrate ($Cu_2NO_3(OH)_3$) was formed, again suggesting the establishment of oxidizing surface redox conditions sufficient to cause oxidative breakdown of the Cu_2O base layer and the incorporation of radiolytically-generated NO_3^- into the corrosion product.

In experiments at very low dose rates (0.35 Gy/h) close to those anticipated under DGR conditions (70% and 85% RH, 70°C),[25] the corrosion process exhibited similar features, the formation of a generally protective Cu_2O layer with local patches within which this layer appeared ruptured, leading to more extensive corrosion and the formation of Cu^{2+} deposits. Whether or not these patches formed depended primarily on the RH, occurring more extensively at the higher RH, but the number of such locations also increased in the presence of radiation.

Cu corrosion driven by both NO_3^- and O_2 reduction will lead to the consumption of H^+. For each dissolved Cu^{2+} species produced by O_2 reduction, $4H^+$ or $2H^+$ will be consumed[26-28] regardless of whether the O_2 is fully reduced to H_2O,

$$O_2 + 4H^+ + 4e^- \rightarrow 2H_2O \quad (1)$$

or if some fraction of the O_2 is only partially reduced to H_2O_2,

$$O_2 + 2H^+ + 2e^- \rightarrow H_2O_2 \quad (2)$$

The reduction of NO_3^- is a multistep reaction which will consume $9H^+$ and $8e^-$ if complete reduction to NH_3 occurs,

$$NO_3^- + 9H^+ + 8e^- \rightarrow NH_3 + 3H_2O \quad (3)$$

However, the conditions under which complete reduction can be achieved have not been resolved.[26,28-31] In acidic solutions, at applied potentials approaching E_{corr}, electrochemical experiments indicate the reaction will be limited to one involving only the first two e^- leading to NO_2^- formation and the consumption of $2H^+$,

$$NO_3^- + 2H^+ + 2e^- \rightarrow NO_2^- + H_2O \quad (4)$$

While these studies yield information on the influence of radiation on Cu corrosion, they have not elucidated the corrosion mechanisms in sufficient detail that models predicting the extent of radiolytic corrosion of Cu under DGR conditions can be developed. In this paper, a study of Cu corrosion in simulated aerated vapor is presented. The primary goal is to investigate the consequences of the radiolytic production of HNO_3 and its absorption by condensed H_2O on the corrosion of Cu high-level nuclear waste containers. The progress of corrosion was monitored by following changes of pH in small, limited volumes of solution. While the solution volume used in the experiments (1.5 mL) was large compared to that anticipated in a condensed H_2O layer or in wet areas on a Cu container surface, it enabled study of the corrosion process up to the establishment of a steady-state condition.

EXPERIMENTAL

Electrode Materials and Preparation

Specimens were cut from an O-free, P-doped, Cu block supplied by SKB† (Svensk Kärnbränslehantering AB).

Cu coupons for microcell experiments were cut as 100 mm long cylinders and the top circular surface mechanically polished prior to an experiment using a series of SiC papers from P800 to P2400 grit. The cylinder was then wrapped in PTFE tape, leaving only the top surface exposed. Heated PTFE heat shrink tubing was then placed over the Cu cylinder and allowed to shrink and form a seal to the PTFE tape, Figure 2. A solution volume of 1.5 mL was used in each experiment. After each experiment, a 5 mm thick disc was mechanically cut from the top of the Cu cylinder to provide a specimen for analyses of the corroded surface.

† Trade name.

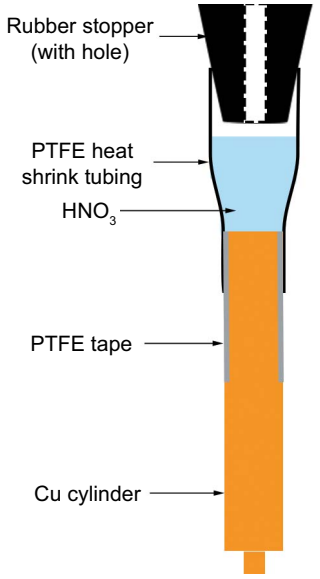

FIGURE 2. *Schematic of microcell arrangement.*

Solutions

All solutions were prepared using Type-1 water from a Barnstead Nanopure† (Thermoscientific) water purification system with a resistivity of 18.2 MΩ·cm. All HNO_3 solutions were prepared by adding specific volumes of a stock solution prepared using HNO_3 (supplied by Caledon†) and Type-1 H_2O. Aerated experiments were performed with the microcell, Figure 2, open to the atmosphere, ensuring a continuous presence of dissolved O_2 in the solution. Experiments under anoxic conditions were performed in an Innovative Technology PureLab HE† Ar-filled glovebox. The minimum measurable $[O_2]$, set by the detection limit of the O_2 sensor in the chamber, was 0.1 ppm. Using a Henry's law constant of 7.79×10^4 L·kPa/mol at 298 K, the dissolved $[O_2]$ was estimated to be ≤ 0.0042 ppb.

Experimental Procedures

The solution pH was measured periodically by temporarily removing the rubber stopper from the microcell and inserting an Orion 9110DJWP Double Junction pH Electrode†, Figure 2. Care was taken to avoid contact of the pH probe with the Cu surface. On completion of an experiment, the cell was dismantled and the corroded surface washed with Type-1 H_2O. A section ~5 mm thick was then cut from the surface for analyses. The freshly exposed surface was then re-prepared as described above.

Analytical Procedures

Scanning electron microscopy (SEM) analyses were performed using a Hitachi SU3500 Variable Pressure† SEM equipped with a Quartz PCI XOne SSD† x-ray analyzer. An electron beam with an

accelerating voltage ranging between 15 kV and 25 kV and a working distance of 10 mm was used to collect high-resolution images at various magnifications. Focused ion beam (FIB) cross sections were performed using a LEO (Zeiss) 1540XB† FIB/SEM at the Western Nanofabrication Facility. An electron beam with an accelerating voltage of 5 kV and a working distance of 20 mm was used to collect high-resolution images of the milled samples at various magnifications.

Raman spectra were obtained using a Renishaw 2000† Raman spectrometer equipped with a 633 nm He-Ne laser and an Olympus† microscope. Images were collected using a 50× uncoated objective lens with the beam focused to a diameter of ~2 μm. The power of the laser beam at the sample surface was kept to 10% to avoid laser heating effects. All spectra were calibrated against the 520.5 cm^{-1} peak of Si.

On completion of an experiment, the 1.5 mL of HNO_3 used in the microcell experiments was placed in a glass vial and analyzed by inductively coupled plasma mass spectrometry (ICP-MS) to determine the concentration of dissolved Cu. All ICP-MS analyses were performed using an Agilent Model 7700† ICP-MS.

The depth of grain boundary etching and the degree of surface roughness were investigated using a Park Systems XE-100† atomic force microscope (AFM).

Optical images were collected using a Leica DVM6† digital microscope.

RESULTS AND DISCUSSION

Figure 3 shows the evolution of pH with exposure time, measured in the microcell, for a number of HNO_3 concentrations ranging from 10 mM to 150 mM. The initial pH is that expected based on the initial HNO_3 concentration. Subsequently, as corrosion proceeds, driven by one or more of the available proton-consuming cathodic reactions (Reactions [1] through [4] above), the pH changes slowly at a rate dependent on the initial H^+ "reservoir" before increasing approximately exponentially. This increase is arrested at a pH value between 3.7 and 3.4 which, as indicated by the horizontal line in Figure 3, is close to the pK_a for the HNO_2 dissociation reaction:[32]

$$HNO_2 \leftrightarrow NO_2^- + H^+ \quad (5)$$

The duration of this arrest, and the pH at which it occurs, varies only slightly with the initial [HNO_3]. The observation that HNO_2 is present indicates that NO_3^- reduction is occurring although, as will be demonstrated below, O_2 reduction is also occurring. Beyond the buffered region, a second increase in pH is observed indicting that corrosion is continuing until a final steady-state value between 4.5 and 5.1 is achieved, with the lower values again reflecting the larger overall H^+ inventories available at the higher initial [HNO_3] values.

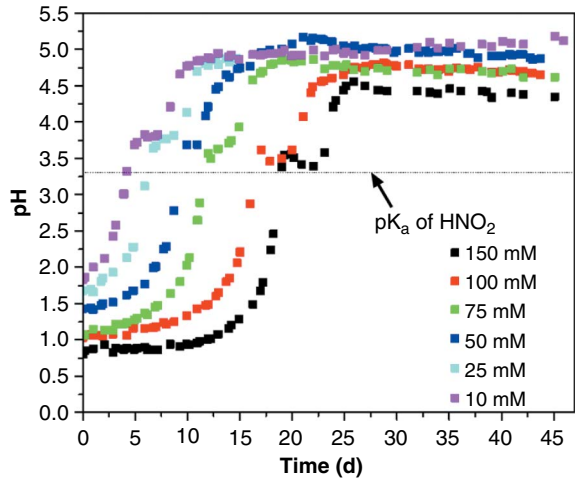

FIGURE 3. *Evolution of pH as a function of time for various initial [HNO_3].*

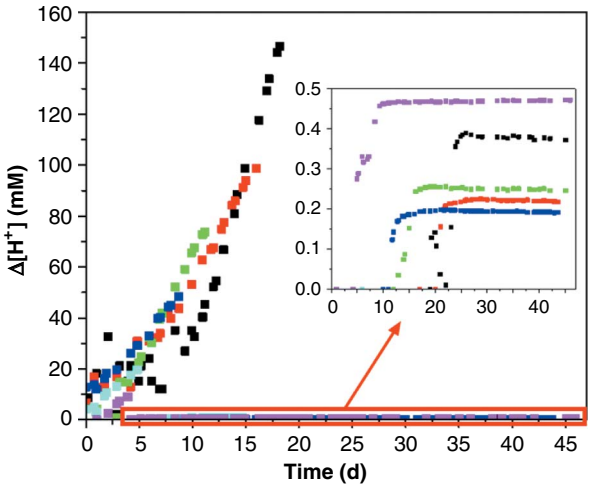

FIGURE 4. *Proton consumption as a function of time. The inset shows an amplification of proton consumption after the pH buffer region (Figure 3).*

The role of the precipitation of copper oxides in determining this final pH are discussed in more detail below.

The amount of H^+ consumed (in mM), $\Delta[H^+]$, can be calculated from the difference between the initial H^+ inventory and the amount of H^+ remaining after an exposure period (t). The slopes of the $\Delta[H^+]$ consumption plots, Figure 4, yield a measure of the rate of consumption ($\Delta[H^+]/\Delta t$) plotted as a function of the initial [HNO_3] in Figure 5. To obtain a measure of reproducibility, the experiment for an initial [HNO_3] of 100 mM was repeated seven times, yielding an average value of 8.40±2.37 mM/d. While the low precision associated with this value may illustrate the variability in the kinetics of the corrosion reaction and possibly variations in the relative importance of the two

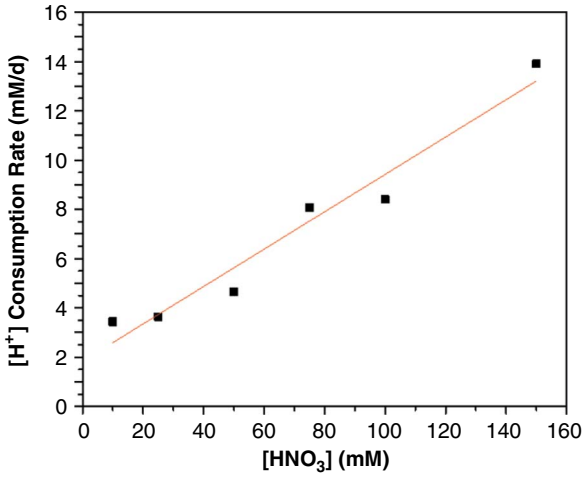

FIGURE 5. *The [H⁺] consumption rate as a function of the initial [HNO_3] in the microcell.*

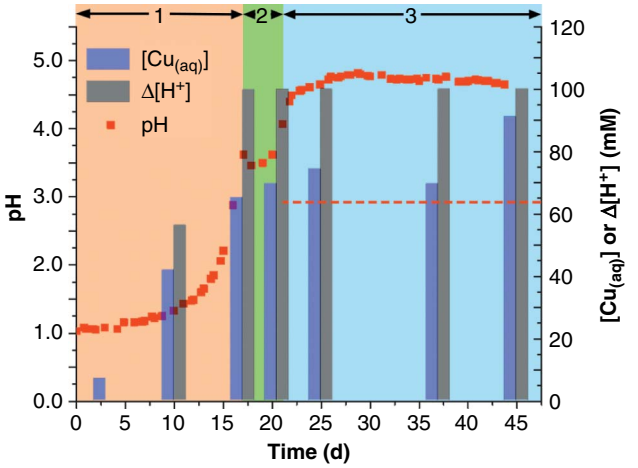

FIGURE 6. *Evolution in pH, [$Cu_{(aq)}$], and Δ[H^+] in the microcell in a solution containing 100 mM HNO_3. Three distinct stages of corrosion are numbered. The dotted red line in Stage 3 indicates the solubility limit for $Cu_{(aq)}$.*

possible cathodic reactions, it will also contain some error associated with the measurement of pH at the lower values.

The dependence of Δ[H^+]/Δt on the initial [HNO_3] could be attributed to either or both of two influences: a dependence of the corrosion rate on [NO_3^-]; and/or a pH dependence of the corrosion rate driven by O_2 reduction. Close inspection of Figure 5 suggests the rate may become independent of pH and/or [HNO_3] for [HNO_3] < 30 mM, although, a more extensive series of measurements is required to confirm whether this is the case.

Once the buffer capacity of HNO_2 is exhausted (pH 3.7 to 3.4), the pH increases further, indicating a continuation of the corrosion reaction (Figure 3). To calculate the [H^+] consumption rates in this exposure period, values of Δ[H^+] were calculated by subtracting the [H^+] in the buffered region from the subsequent measured values of [H^+]. The proton consumption values (Δ[H^+]) obtained are plotted as a function of time in the inset in Figure 4. No significant variations in slope (Δ[H^+]/Δt) with initial [HNO_3] are observed and only small changes in Δ[H^+] occur before [H^+] consumption ceases.

To investigate the evolution of the corrosion process as the pH changes, a series of identical microcell experiments were conducted in aerated solutions containing 100 mM of HNO_3. Individual experiments were stopped at different times, the pH measured, and the concentration of dissolved Cu (Cu_{aq}) analyzed. The pH-exposure time plot (from Figure 3) and the Δ[H^+] values and [Cu_{aq}] from the individual experiments are compared in Figure 6. Three distinct regions of behavior are apparent.

The first stage (light red in Figure 6) encompasses the exposure period within which the pH increases exponentially. To check that this series of experiments can be legitimately compared to that from Figure 3, the [H^+] consumption rate was calculated from the initial and final pH values for three individual experiments that were stopped at different stages of the pH evolution. Assuming a linear decrease in [H^+], an average value of 7.3±1.15 mM/d was obtained. This is well within the range of values of 8.4±2.37 mM/d, measured in the previous experiments. As expected, the [Cu_{aq}] also increases over this exposure period at an average rate of 4.14 mM/d. Based on the E-pH diagram for Cu[26,33] and the relative solubilities of Cu^+ and Cu^{2+} in the pH range 1 to 3.5, dissolution of cations in both oxidation states can occur, with Cu^{2+} expected to dominate.

Stage 2 (green in Figure 6) corresponds to the region in which the pH is buffered by Reaction (5). Although no change in [H^+] can be measured, the increase in [Cu_{aq}] indicates corrosion continues but at a much lower rate, a possible indication that [Cu_{aq}] is approaching or has exceeded a solubility limit. The final stage (blue in Figure 6) encompasses the region within which [H^+] consumption ceases. The [Cu_{aq}] also appears to stabilize, although the high value observed after 45 d prevents a definite conclusion. Based on the solubility-pH diagram for the dominant solution species, Cu^{2+},[34] the solubility at the final pH of 4.6 is calculated to be ~63 mM, which is close to the measured [Cu_{aq}] values as indicated by the dashed line in Figure 6, indicating the solubility limit for Cu^{2+} is reached in this region. Because neither Cu^+ nor Cu^{2+} are significantly hydrolyzed at pH = 4.6, buffering of the pH by hydrolysis equilibria, which would allow corrosion to continue without an observable change in pH and [Cu_{aq}], is not a feasible process, indicating that corrosion ceases when the solubility limit is reached.

Specimens removed during the various stages (defined in Figure 6) show that the nature of the

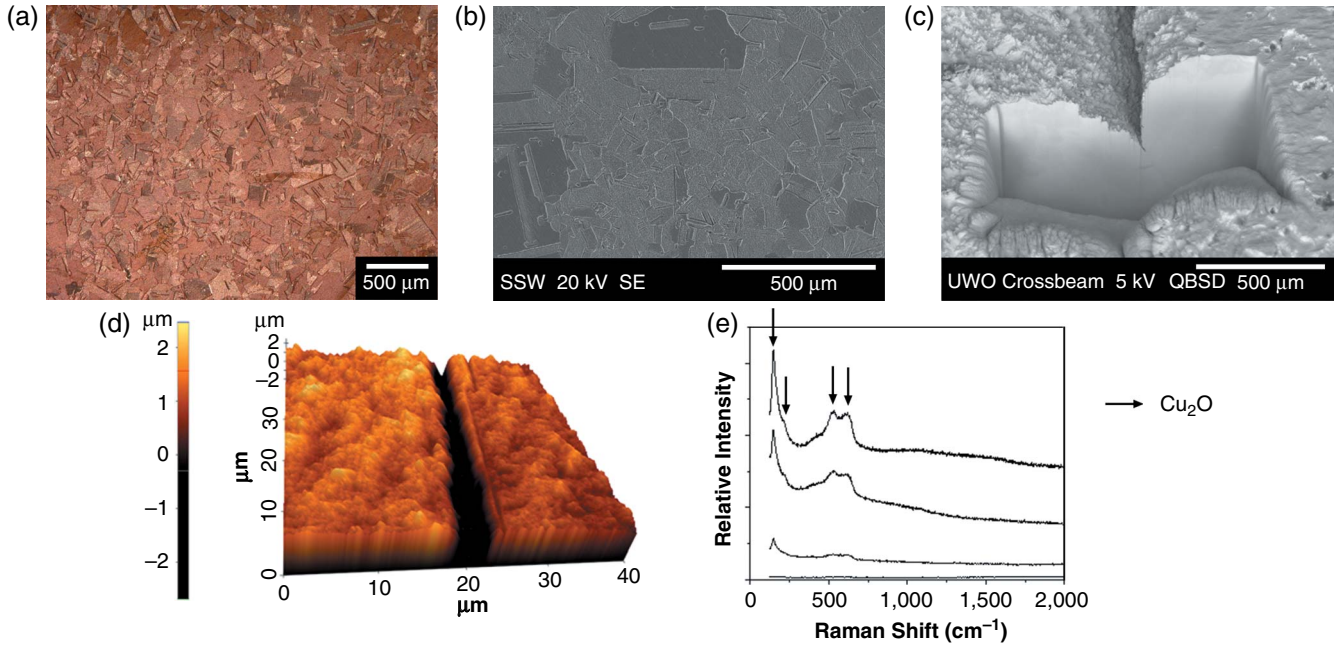

FIGURE 7. *Analysis of a Cu surface corroded in a solution containing 100 mM HNO_3 (10 d). (a) Optical and (b) SEM images showing the etched Cu surface; (c) a FIB cross-section image and (d) an AFM map of a preferentially etched grain boundary; and (e) Raman spectra, indicating the presence of a thin Cu_2O oxide.*

corrosion process evolves with time. The optical and SEM images, Figures 7(a) and (b), recorded on the specimen corroded for 10 d, show extensive damage, with some grains more damaged than others, confirming that extensive corrosion occurs throughout Stage 1. Some grain boundaries are preferentially dissolved, as shown by the AFM image, Figure 7(d), and the FIB-cut cross section in Figure 7(c). In the latter case, this probably reflects the different dissolution rates of the adjacent grains, the height difference between the two grains being ~3 µm. The AFM map depicts two grains corroding at similar rates, with preferential etching of the grain boundary occurring to a depth of ~3 µm. These observations are consistent with published studies showing similar etching in acidic solutions.[35]

Figure 7(e) shows a series of Raman spectra recorded at various locations on the corroded surface. The peaks at 525 cm^{-1}, 625 cm^{-1}, 147 cm^{-1}, and the faint peak at 220 cm^{-1} indicate the presence of Cu_2O.[20-23,36-39] The detection of this phase in the absence of any discrete deposited crystals suggests Cu_2O is present as a pervasive surface film. Given the roughness of the corroded surface, it is possible these Raman responses are surface-enhanced[29] and that the variations in peak intensities reflect the different corrosion rates on different crystal faces, with strong signals surface enhanced.

While the dissolution of Cu can lead to both soluble Cu^+ and Cu^{2+},[26,33] the latter is considerably more soluble in acidic solutions and, hence, the expected dissolution product. Additionally, dissolved Cu^+ is likely to undergo homogeneous irreversible oxidation to Cu^{2+} in an aerated solution:[40]

$$4Cu^+ + O_2 + 2H_2O \rightarrow 4Cu^{2+} + 4OH^- \quad (6)$$

Consequently, two processes could account for the presence of a Cu_2O surface layer: (i) the phase is formed and partially stabilized on the Cu surface by reaction with NO_3^- (as described above) and is an intermediate in the anodic dissolution process to produce Cu^{2+}; or (ii) large concentrations of Cu^{2+} are unstable in the presence of Cu and react to form Cu_2O.[41]

In Stage 2, when [Cu_{aq}] is considerably higher (after 17 d) and corrosion is continuing, a scattered, unprotective corrosion product deposit is observed. In the optical and SEM images, Figures 8(a) and (b), the etched morphology of the Cu substrate remains visible at locations not covered by corrosion product. The dark blue areas in the optical image, Figure 8(a), indicate the location of the large crystals (≥ 50 µm in dimension) like the one shown in Figure 8(b). Cuprite is known to form many derivatives of cubic structures, suggesting such truncated cubic structures are Cu_2O.[42-45]

The SEM image, Figure 8(c), also shows the presence of smaller cubic oxide particles with dimensions ranging from 2 µm to 10 µm. FIB-cut cross sections of these cubes, Figure 8(d), shows they are strongly adherent to the Cu surface. SEM/EDS (energy dispersive x-ray spectroscopy) analyses suggest they are Cu_2O.[42-45] This is confirmed by the Raman spectra in Figure 8(e), which exhibit strong signals at

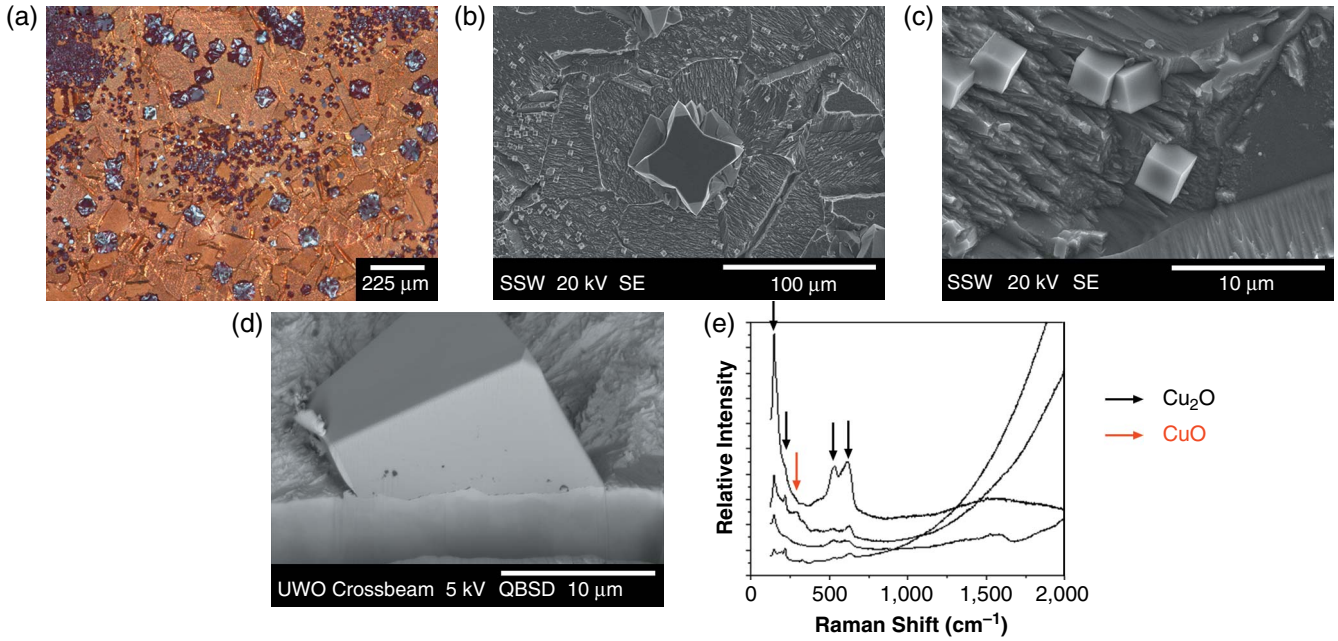

FIGURE 8. *Analysis of a Cu surface after corrosion in a 100 mM HNO_3 solution for 17 d. (a) Optical and ([b] and [c]) SEM images showing the various Cu_2O oxide forms; (d) a FIB-cut cross section showing the oxide is strongly adherent to the Cu surface; and (e) Raman spectra indicating the presence of Cu_2O and possibly CuO.*

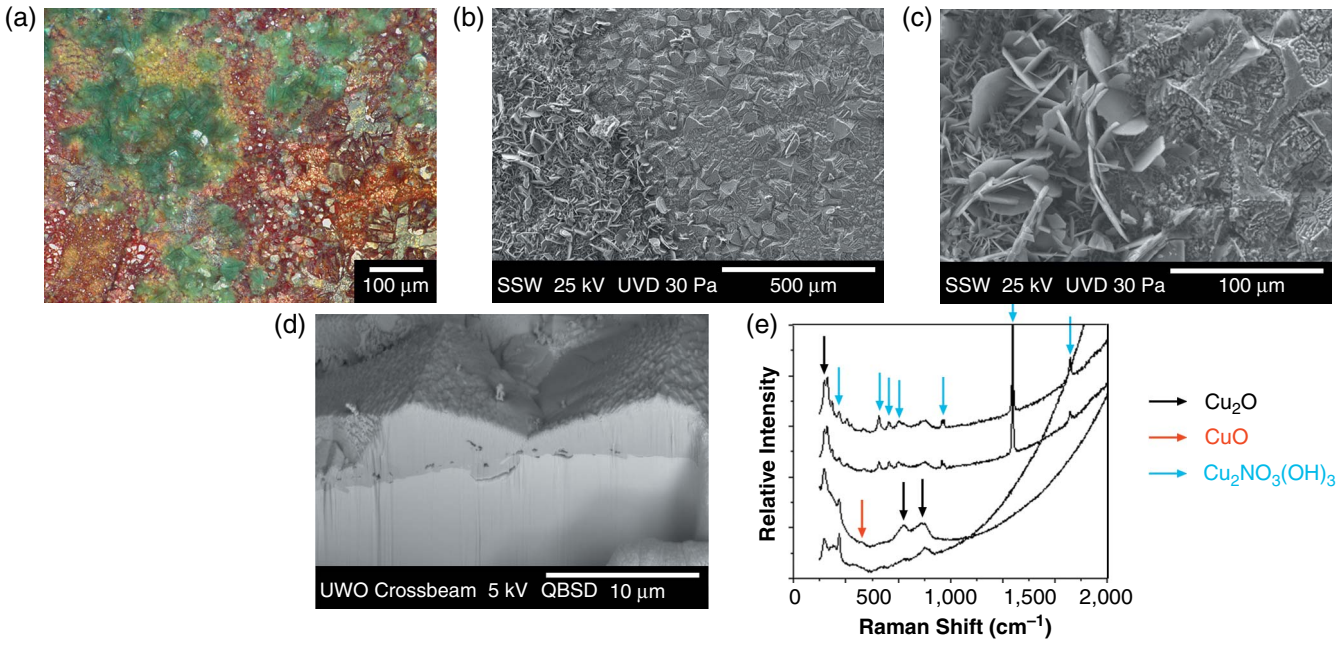

FIGURE 9. *Analysis of a Cu surface corroded in a 100 mM solution of HNO_3 for 37 d. (a) Optical and ([b] and [c]) SEM images showing forms of the Cu_2O and $Cu_2NO_3(OH)_3$ deposits; (d) a FIB-cut cross section indicating the oxide forms a protective surface layer; and (e) Raman spectra indicating the presence of Cu_2O, $Cu_2NO_3(OH)_3$, and possibly CuO.*

the locations of large crystals and weaker signals accompanied by high levels of fluorescence at locations covered by scattered small cubes. Although too small to unequivocally identify by Raman spectroscopy,[46] the shape of these small cubes suggest they are Cu_2O.[42-45] The very weak signal at 297 cm^{-1} yields the first indication of the formation of CuO.[37,47-48] This observation is consistent with the expected [Cu_{aq}], which is close to the solubility limit for Cu^{2+} in this region. Given the relative solubilities of Cu^+ and Cu^{2+}, the earlier deposition of Cu_2O is expected.

For a specimen removed in Stage 3 (after 37 d), the etched Cu substrate surface can no longer be seen in either optical, Figure 9(a), or SEM images, Figures 9(b) and (c), the surface being covered by a compact featureless Cu_2O layer with patches of light blue (Figure 9[a]) rouaite ($Cu_2NO_3(OH)_3$) platelets, Figure 9(c). Raman spectra, Figure 9(e), confirm the dominant surface phase is Cu_2O with a minor signal for CuO. Raman spectra collected at the light blue locations in the optical image show peaks for both rouaite[46,49] and Cu_2O, confirming that the Cu^{2+} phase is deposited on the surface of a Cu_2O layer. Examination of the FIB-cut cross section, Figure 9(d), shows that the Cu_2O layer present at the pH prevailing in this region, at which the solubility of Cu^+ will be significantly reduced, is compact and protective. As noted above, and illustrated in Figure 6, the solubility limit for Cu^{2+} at the pH prevailing in this region is also exceeded. That Cu^{2+} co-precipitates with NO_3^- and OH^-[50-51] confirms that unreduced NO_3^- remains in the solution despite the extensive H^+ consumption, leading to a sufficiently high pH for this co-precipitation of Cu^{2+}, NO_3^-, and OH^-.

In an attempt to determine the relative importance of the two possible cathodic reactions, a series of experiments (10) were conducted in 100 mM HNO_3 in the absence of dissolved O_2 in an anaerobic chamber for various durations. No measurable H^+ consumption was observed in any of the experiments including one that lasted for 363 d, Figure 10. To emphasize the contrast with the rapid H^+ consumption under aerated conditions, the plot for this [HNO_3] (from Figure 3) is also included. SEM micrographs, Figure 11, show corrosion was unobservable over the first 120 d of exposure despite the presence of the potential oxidant, HNO_3. After 230 d, shallow pitting was observed which evolved after 363 d into a more general roughening of the surface, generally associated with the polishing lines. The very slow rate of corrosion is confirmed by ICP-MS analyses of the dissolved Cu concentration in the microcell, which increases from 1.8 mM after 120 d to 3.2 mM after 363 d. This can be compared to the 70 mM to 90 mM concentrations, accompanied by the copious deposition of corrosion products, observed after 25 d to 45 d when dissolved O_2 is present. Assuming a linear accumulation of dissolved Cu with exposure time yields a Cu release rate of

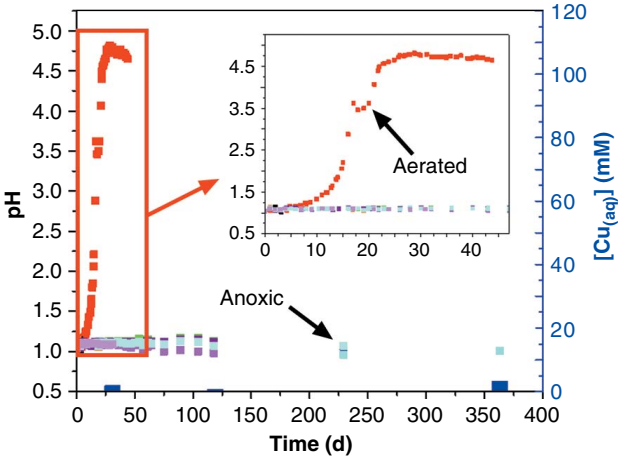

FIGURE 10. *Change in pH and [$Cu_{(aq)}$] in a series of experiments (of various durations) in an anoxic 100 mM HNO_3 solution compared to the changes observed in an aerated 100 mM HNO_3 solution (from Figure 6 [outlined in red]). The inset shows a magnification of the first 45 d.*

0.010 mM/d to 0.015 mM/d compared to 4.14 mM/d under aerated conditions, a decrease by a factor of ~280 to ~460.

This behavior shows that corrosion is inhibited in HNO_3 solutions consistent with literature claims that NO_3^- reduction is difficult to induce on Cu surfaces.[28,30] A number of studies have shown that, depending on the Cu crystal plane, NO_3^- reduction is either completely blocked or proceeds very slowly.[29,52] Based on AFM and enhanced Raman spectroscopy studies, this was attributed to either the chemisorption of NO_3^- or to the formation of Cu_2O by the extraction of an O atom from adsorbed NO_3^-. The formation of these species, especially a Cu_2O layer, would be consistent with this study's Raman spectroscopic observations.

This comparison between the corrosion behavior in anoxic and aerated environments clearly demonstrates that dissolved O_2 is the dominant oxidant. However, the observation that HNO_2 is formed in aerated solutions confirms NO_3^- reduction is also occurring to a greater extent than observed under anoxic conditions. A possible explanation for such an activation process would be production of Cu^+ as a surface intermediate. This species has been shown to act as a catalyst for NO_3^- reduction on Cu surfaces.[28-29,53] However, because Cu^+ is considerably less soluble than Cu^{2+} in the pH range of these experiments,[34,54] it is likely to have only a transient lifetime as a surface species before further oxidation to the soluble Cu^{2+}, a reaction which appears to occur dominantly by reaction with dissolved O_2.

In the absence of O_2, corrosion is very significantly reduced as a result of the formation of chemisorbed NO_3^- and/or NO_2^-, and/or Cu_2O. These surface

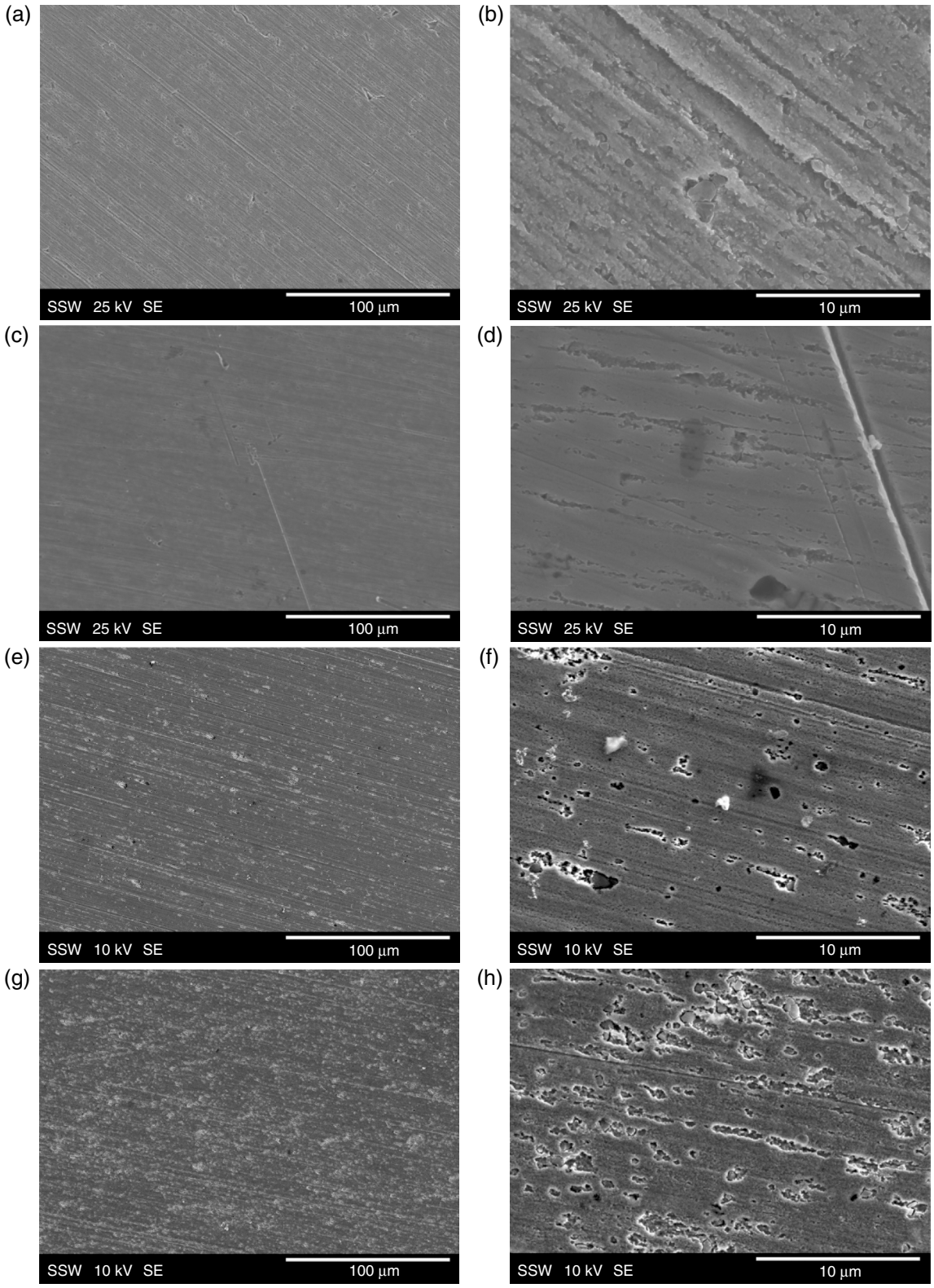

FIGURE 11. *SEM micrographs of Cu coupons after immersion in 100 mM HNO_3 in an anaerobic chamber for ([a] and [b]) ~31 d; ([c] and [d]) ~119 d; ([e] and [f]) ~230 d; and ([g] and [h]) ~363 d.*

species are only marginally protective, with corrosion slowly leading to a more general roughening of the Cu surface. In the microcell, the ready availability of O_2 would maintain the production of Cu^+ and, hence, the catalysis of NO_3^- reduction, leading to the formation of soluble Cu^{2+}.

SUMMARY AND CONCLUSIONS

❖ The corrosion of Cu has been studied in small volumes of HNO_3 solution to simulate the influence of the radiolytic production of HNO_3 in aerated water vapor.

❖ In the presence of deaerated HNO_3, only minor surface roughening occurred, the initial rapid reduction of HNO_3 leading to a marginally reactive surface by either the formation of chemisorbed NO_3^- and NO_2^- and/or the formation of a thin Cu_2O layer.

❖ When O_2 was present, corrosion was markedly accelerated with O_2 initially acting as the dominant cathodic reactant. This led to the activation of HNO_3 as a cathodic reactant, a process which appeared to involve the catalytic influence of Cu^+.

❖ While corrosion was initially very rapid, saturation of the limited volume of solution eventually led to stifling of the corrosion process by the accumulation of Cu_2O and, to a limited extent, CuO.

❖ Unreduced NO_3^- was eventually precipitated on the Cu_2O/Cu surface once saturation with dissolved Cu^{2+} was achieved.

❖ While these results establish a feasible mechanism for the corrosion of Cu in aerated HNO_3, the absence of clay sealing material precludes their direct application to deep geologic repository conditions.

ACKNOWLEDGMENTS

This project was funded under a collaborative research and development grant funded by the Canadian Natural Sciences and Engineering Research Council (NSERC) and the Nuclear Waste Management Organization (NWMO, Toronto). We are grateful to the Swedish Nuclear Fuel and Waste Management Company (Stockholm) for the donation of copper material.

REFERENCES

1. F. Garisto, "Fourth Case Study: Features, Events, and Processes," Nuclear Waste Management Organization Technical Report, NWMO-TR-2012-14, 2012.
2. G.M. Kwong, "Status of Corrosion Studies for Copper Used Fuel Containers Under Low Salinity Conditions," Nuclear Waste Management Organization Technical Report, NWMO-TR-2011-14, 2011.
3. J.R. Scully, M. Edwards, "Review of the NWMO Copper Corrosion Allowance," Nuclear Waste Management Organization Technical Report, NWMO-TR-2013-04, 2013.
4. P.G. Keech, P. Vo, S. Ramamurthy, J. Chen, R. Jacklin, D.W. Shoesmith, *Corros. Eng. Sci. Technol.* 49, 6 (2014): p. 425-430.
5. F. King, C. Lilja, K. Pedersen, P. Pitkanen, M. Vahanen, "An Update of the State-of-the-Art Report on the Corrosion of Copper Under Expected Conditions in a Deep Geologic Repository," Svensk Kärnbränslehantering AB Technical Report, SKB-TR-10-67, 2010.
6. C.H. Boyle, S.A. Meguid, *Nucl. Eng. Des.* 293 (2015): p. 403-412.
7. C. Leygraf, "Atmospheric Corrosion," in *Corrosion Mechanisms in Theory and Practice*, eds. P. Marcus, J. Oudar (New York, NY: Marcel Dekker Inc., 2000).
8. F. King, D.S. Hall, P.G. Keech, *Corros. Eng. Sci. Technol.* 52, supplement 1 (2017): p. 25-30.
9. T. Standish, J. Chen, R. Jacklin, P. Jakupi, S. Ramamurthy, D. Zagidulin, P. Keech, D. Shoesmith, *Electrochim. Acta* 211 (2016): p. 331-342.
10. G.R.A. Johnson, "The Radiation Chemistry of Nitrogen and Its Compounds," in *Inorganic and Theoretical Chemistry* (New York, NY: John Wiley & Sons, 1967).
11. S. Sato, M. Steinberg, "Radiation Chemical Nitrogen Fixation in Air-Water Systems," Brookhaven National Lab, BNL–13692, March 1969.
12. R.S. Wittman, "Radiolysis Model Sensitivity Analysis for a Used Fuel Storage Canister," Pacific Northwest National Laboratory, PNNL-22773, 2013.
13. P.A. Yakabuskie, J.M. Joseph, J.C. Wren, *Radiat. Phys. Chem.* 79, 7 (2010): p. 777-785.
14. P.A. Yakabuskie, J.M. Joseph, C.R. Stuart, J.C. Wren, *J. Phys. Chem. A* 115, 17 (2011): p. 4270-4278.
15. R.P. Morco, J.M. Joseph, D.S. Hall, C. Medri, D.W. Shoesmith, J.C. Wren, *Corros. Eng. Sci. Technol.* 52, supplement 1 (2017): p. 141-147.
16. C. Donohoe, "The Effect of Ionising Radiation on the Corrosion Resistance of Ilw Containers," National Nuclear Laboratory Report, NNL (08) 9544, Issue 3, 2009.
17. D.W. Shoesmith, F. King, "The Effects of Gamma Radiation on the Corrosion of Candidate Materials for the Fabrication of Nuclear Waste Packages," Atomic Energy of Canada Limited Report, AECL-11999, 1999.
18. F. King, C. Litke, "The Corrosion of Copper in Synthetic Groundwater at 150 C. Part I. The Results of Short Term Electrochemical Tests," Atomic Energy of Canada Limited, AECL-TR-428, 1987.
19. F. King, C. Litke, K. George, "The Corrosion of Copper in Synthetic Groundwater at 150 C. Part II. The Characterization of Surface Films," Atomic Energy of Canada Limited, AECL-TR-464, 1989.
20. J. Simpson, P. Valloton, "Experiments on Container Materials for Swiss High-Level Waste Disposal Projects Part III," Nagra Technical Report, Technical Report 86 25, 1984.
21. Å. Björkbacka, S. Hosseinpour, M. Johnson, C. Leygraf, M. Jonsson, *Radiat. Phys. Chem.* 92 (2013): p. 80-86.
22. Å. Bjorkbacka, M. Yang, C. Gasparrini, C. Leygraf, M. Jonsson, *Dalton Trans.* 44, 36 (2015): p. 16045-16051.
23. Å. Björkbacka, C.M. Johnson, C. Leygraf, M. Jonsson, *J. Phys. Chem. C* 120, 21 (2016): p. 11450-11455.
24. D.T. Reed, R.A. Van Konynenburg, "Corrosion of Copper-Based Materials in Irradiated Moist Air Systems," in *MRS Proceedings*, vol. 212 (Cambridge, United Kingdom: Cambridge University Press, 1990), p. 317.
25. B. Ibrahim, D. Zagidulin, J.M. Smith, S. Ramamurthy, J.C. Wren, D.W. Shoesmith, "Radiolytic Corrosion of Cu Nuclear Waste Containers," 17th International Conference in Environmental Degradation of Materials in Nuclear Power Systems (Ottawa, Ontario: Curran Associates, Incorporated, 2015).
26. K.F. Khaled, *Corros. Sci.* 52, 10 (2010): p. 3225-3234.
27. H. Ma, S. Chen, B. Yin, S. Zhao, X. Liu, *Corros. Sci.* 45, 5 (2003): p. 867-882.
28. E.V. Filimonov, A.I. Shcherbakov, *Prot. Met.* 40, 3 (2004): p. 280-285.
29. S.-E. Bae, K.L. Stewart, A.A. Gewirth, *J. Am. Chem. Soc.* 129, 33 (2007): p. 10171-10180.
30. G.E. Dima, A.C.A. de Vooys, M.T.M. Koper, *J. Electroanal. Chem.* 554-555 (2003): p. 15-23.
31. U. Prüsse, M. Hähnlein, J. Daum, K.-D. Vorlop, *Catal. Today* 55, 1-2 (2000): p. 79-90.
32. W.M. Haynes, *CRC Handbook of Chemistry and Physics*, 95th ed., vol. 95 (Boca Raton, FL: Taylor and Francis, 2014).
33. B. Beverskog, I. Puigdomenech, *J. Electrochem. Soc.* 144, 10 (1997): p. 3476-3483.
34. C.F. Baes, R.E. Mesmer, *Hydrolysis of Cations* (Malabar, FL: Robert E. Krieger Publishing Company, Inc., Wiley, 1976).

35. E. Martinez-Lombardia, L. Lapeire, V. Maurice, I. De Graeve, K. Verbeken, L. Klein, L. Kestens, P. Marcus, H. Terryn, *Electrochem. Commun.* 41 (2014): p. 1-4.
36. P. Ropret, T. Kosec, *J. Raman Spectrosc.* 43, 11 (2012): p. 1578-1586.
37. R.L. Frost, *Spectrochim. Acta A* 59, 6 (2003): p. 1195-1204.
38. R.L. Frost, W. Martens, J.T. Kloprogge, P.A. Williams, *J. Raman Spectrosc.* 33, 10 (2002): p. 801-806.
39. F. Texier, L. Servant, J. Bruneel, F. Argoul, *J. Electroanal. Chem.* 446, 1 (1998): p. 189-203.
40. V.K. Sharma, F.J. Millero, *J. Solution Chem.* 17, 6 (1988): p. 581-599.
41. D.G. Peters, S.A. Cruser, *J. Electroanal. Chem. (1959)* 9, 1 (1965): p. 27-40.
42. M.J. Siegfried, K.-S. Choi, *J. Am. Chem. Soc.* 128, 32 (2006): p. 10356-10357.
43. Y. Sui, W. Fu, H. Yang, Y. Zeng, Y. Zhang, Q. Zhao, Y. Li, X. Zhou, Y. Leng, M. Li, G. Zou, *Cryst. Growth Des.* 10, 1 (2010): p. 99-108.
44. K. Chen, C. Sun, S. Song, D. Xue, *CrystEngComm* 16, 24 (2014): p. 5257-5267.
45. I. Sakellis, S. Giamini, I. Moschos, C. Chandrinou, A. Travlos, C.Y. Kim, J.H. Lee, J.G. Kim, N. Boukos, *Energy Procedia* 60 (2014): p. 37-42.
46. M. Bouchard, D.C. Smith, *Spectrochim. Acta A* 59, 10 (2003): p. 2247-2266.
47. J.C. Hamilton, J.C. Farmer, R.J. Anderson, *J. Electrochem. Soc.* 133, 4 (1986): p. 739-745.
48. H. Hagemann, H. Bill, W. Sadowski, E. Walker, M. François, *Solid State Commun.* 73, 6 (1990): p. 447-451.
49. V. Bongiorno, S. Campodonico, R. Caffara, P. Piccardo, M.M. Carnasciali, *J. Raman Spectrosc.* 43, 11 (2012): p. 1617-1622.
50. C. Yoder, E. Bushong, X. Liu, V. Weidner, P. McWilliams, K. Martin, J. Lorgunpai, J. Haller, R. Schaeffer, *Mineral. Mag.* 74, 3 (2010): p. 433-440.
51. C.H. Yoder, N.R. Gotlieb, A.L. Rowand, *Am. Mineral.* 95, 1 (2010): p. 47-51.
52. S.-E. Bae, A.A. Gewirth, *Faraday Discuss.* 140 (2008): p. 113-123.
53. J. Davis, M.J. Moorcroft, S.J. Wilkins, R.G. Compton, M.F. Cardosi, *Analyst* 125, 4 (2000): p. 737-742.
54. D. Palmer, *J. Solution Chem.* 40, 6 (2011): p. 1067-1093.